



HAL
open science

Electron diffusion region during magnetopause reconnection with an intermediate guide field: Magnetospheric multiscale observations

L. -J. Chen, M. Hesse, S. Wang, D. Gershman, R. E. Ergun, J. Burch, N. Bessho, R. B. Torbert, B. Giles, J. Webster, et al.

► To cite this version:

L. -J. Chen, M. Hesse, S. Wang, D. Gershman, R. E. Ergun, et al.. Electron diffusion region during magnetopause reconnection with an intermediate guide field: Magnetospheric multiscale observations. *Journal of Geophysical Research Space Physics*, 2017, 122, pp.5235-5246. 10.1002/2017JA024004 . insu-03677002

HAL Id: insu-03677002

<https://insu.hal.science/insu-03677002>

Submitted on 24 May 2022

HAL is a multi-disciplinary open access archive for the deposit and dissemination of scientific research documents, whether they are published or not. The documents may come from teaching and research institutions in France or abroad, or from public or private research centers.

L'archive ouverte pluridisciplinaire **HAL**, est destinée au dépôt et à la diffusion de documents scientifiques de niveau recherche, publiés ou non, émanant des établissements d'enseignement et de recherche français ou étrangers, des laboratoires publics ou privés.

Copyright

RESEARCH ARTICLE

10.1002/2017JA024004

Special Section:

Magnetospheric Multiscale (MMS) mission results throughout the first primary mission phase

Key Points:

- Motion of demagnetized electrons is key to the reconnection current and collisionless dissipation under the observed guide field
- The guide field modifies the out-of-plane magnetic field pattern and the electron flow dynamics therein
- The reconnection electric field is measured to be ~ 0.1 and uniform over the interspacecraft separation in the magnetosheath EDR and inflow

Correspondence to:

L.-J. Chen,
lijen@mailaps.org

Citation:

Chen, L.-J., et al. (2017), Electron diffusion region during magnetopause reconnection with an intermediate guide field: Magnetospheric multiscale observations, *J. Geophys. Res. Space Physics*, 122, 5235–5246, doi:10.1002/2017JA024004.

Received 6 FEB 2017

Accepted 25 APR 2017

Accepted article online 28 APR 2017

Published online 17 MAY 2017

Electron diffusion region during magnetopause reconnection with an intermediate guide field: Magnetospheric multiscale observations

L.-J. Chen^{1,2} , M. Hesse¹, S. Wang^{1,2} , D. Gershman^{1,2} , R. E. Ergun³ , J. Burch⁴ , N. Bessho^{1,2} , R. B. Torbert^{4,5} , B. Giles¹ , J. Webster⁶ , C. Pollock⁷ , J. Dorelli¹, T. Moore¹ , W. Paterson¹ , B. Lavraud^{8,9} , R. Strangeway¹⁰ , C. Russell¹⁰ , Y. Khotyaintsev¹¹ , P.-A. Lindqvist¹² , and L. Avanov^{1,2} 

¹NASA, Goddard Space Flight Center, Greenbelt, Maryland, USA, ²Department of Astronomy, University of Maryland, College Park, Maryland, USA, ³Laboratory of Atmospheric and Space Sciences, University of Colorado Boulder, Boulder, Colorado, USA, ⁴Southwest Research Institute, San Antonio, Texas, USA, ⁵Department of Physics, University of New Hampshire, Durham, New Hampshire, USA, ⁶Department of Physics and Astronomy, Rice University, Houston, Texas, USA, ⁷Denali Scientific, Healy, Alaska, USA, ⁸Institut de Recherche en Astrophysique et Planétologie, Université de Toulouse, Toulouse, France, ⁹Centre National de la Recherche Scientifique, UMR 5277, Toulouse, France, ¹⁰Earth, Planetary, and Space Sciences, University of California, Los Angeles, California, USA, ¹¹Swedish Institute of Space Physics, Uppsala, Sweden, ¹²KTH Royal Institute of Technology, Stockholm, Sweden

Abstract An electron diffusion region (EDR) in magnetic reconnection with a guide magnetic field approximately 0.2 times the reconnecting component is encountered by the four Magnetospheric Multiscale spacecraft at the Earth's magnetopause. The distinct substructures in the EDR on both sides of the reconnecting current sheet are visualized with electron distribution functions that are 2 orders of magnitude higher cadence than ever achieved to enable the following new findings: (1) Motion of the demagnetized electrons plays an important role to sustain the reconnection current and contributes to the dissipation due to the nonideal electric field, (2) the finite guide field dominates over the Hall magnetic field in an electron-scale region in the exhaust and modifies the electron flow dynamics in the EDR, (3) the reconnection current is in part carried by inflowing field-aligned electrons in the magnetosphere part of the EDR, and (4) the reconnection electric field measured by multiple spacecraft is uniform over at least eight electron skin depths and corresponds to a reconnection rate of approximately 0.1. The observations establish the first look at the structure of the EDR under a weak but not negligible guide field.

1. Introduction

The electron diffusion region (EDR) is the region where electrons are decoupled from the magnetic field and is thought to hold the key to understanding how reconnection occurs in collisionless plasmas [e.g., *Fujimoto and Sydora*, 2009; *Hesse et al.*, 2011; *Mozer and Pritchett*, 2011; *Chen et al.*, 2016a]. Resolving the EDR with electron distribution functions (DFs) is a new capability enabled by the Magnetospheric Multiscale (MMS) mission whose key aim is to study electron-scale physics in magnetic reconnection [*Burch et al.*, 2015]. To date, a number of EDR encounters by MMS have been reported. For the cases with negligible guide fields, the electron DFs from the EDR crossings in both the magnetosphere side [*Burch et al.*, 2016] and the magnetosheath part [*Chen et al.*, 2016b] of the current sheet appear to be consistent with those predicted by particle-in-cell (PIC) simulations [*Hesse et al.*, 2014; *Bessho et al.*, 2016, *Chen et al.*, 2016a, 2016b], suggesting that the EDR physics is predominantly governed by the meandering electrons. For guide fields of one [*Burch and Phan*, 2016] and four [*Eriksson et al.*, 2016] times the reconnecting magnetic field component (B_R), the acceleration by electric fields parallel to the guide field is shown to result in pronounced extensions of the electron DFs to high parallel velocities. In this paper, we report a new EDR encounter with a guide field $\sim 0.2 B_R$, intermediate between the above two documented regimes (negligible and guide-field dominated). The distinct electron regions on both sides of the reconnecting current sheet will be visualized with electron distribution functions from the four MMS spacecraft. The improvement over 2 orders of magnitude on the cadence of the electron distribution measurements is key to the new discoveries to be reported.

Important to the physics of the diffusion region in collisionless reconnection is what contributes to the reconnection current, and how the current is sustained. For magnetopause reconnection with negligible guide

fields, the reconnection current (J_R) is carried by the meandering electrons moving primarily perpendicular to the magnetic field, as revealed by MMS observations [Burch *et al.*, 2016] as well as PIC simulations [Hesse *et al.*, 2014; Chen *et al.*, 2016a; Shay *et al.*, 2016]. For a guide field $\sim 1 B_R$, J_R is shown to be parallel to the guide field in the vicinity of the current sheet midplane [Burch and Phan, 2016]. For the event to be discussed in this paper, J_R will be shown to have both perpendicular and parallel components and to be carried by a combination of meandering and inflowing field-aligned electrons.

2. MMS Data

The observations are from the four-spacecraft mission Magnetospheric Multiscale (MMS) [Burch *et al.*, 2015, Burch *et al.*, 2016a]. The data employed are from burst-mode Fast Plasma Investigation [Pollock *et al.*, 2016], the Fluxgate Magnetometer [Russel *et al.*, 2014], the electric field spin plane [Lindqvist *et al.*, 2014], and axial [Ergun *et al.*, 2016a] double probes in the FIELDS suites [Torbert *et al.*, 2014]. The location of MMS is the Earth's dawn magnetopause at GSM (10.1, -4.2 , -1.2) R_E . All vector quantities will be displayed in the LMN coordinate determined by a hybrid method [e.g., Denton *et al.*, 2016] of Minimum Directional Derivative (MDD) [Shi *et al.*, 2005] and Minimum Variance Analysis (MVA) [Sonnerup and Scheible, 1998]. An initial L_0 direction is derived as the direction of the magnetic field component that exhibits the highest variance over the interval 14 December 2015/01:17:33.5–01:17:44.2 UT, and positive L_0 is defined such that B_L in the magnetosphere side of the current sheet is positive (hence B_L in the magnetosheath side of the current sheet is negative). The N direction is defined to be along the maximum magnetic gradient, positive toward the magnetosheath (different from the N based on MVA by about 20°). $N \times L_0$ determines the M direction. The final L direction is $M \times N$, about 10° from L_0 . The LMN derived based on the above MVA-MDD method has its B_N sign variation consistent with that inferred from the electron DFs. A rotation from the above LMN to the bisection coordinate (obtained by fixing the N direction from MDD and taking the bisection between the upstream B_{LM} components from the magnetosheath and magnetosphere to be the M direction) in which the reconnection rate is thought to maximize [Hesse *et al.*, 2013] does not alter the results in any appreciable way.

3. Results

The EDR encounter occurs in the vicinity of the magnetic field B_N and B_L reversals (Figure 1a), at an intermediate density indicative of mixing of magnetosheath (sheath) and magnetosphere (sphere) plasmas (Figure 1b), and after the passing of an ion jet with peak $V_{iL} \sim -200$ km/s (Figure 1c). The sheath Alfvén speed $V_A \sim 180$ km/s, using the n and $|B|$ from 011735 UT as the sheath upstream. The guide field is estimated to be 20% of the reconnecting component based on $B_L \sim 40$ nT, $B_M \sim -8$ nT at ~ 011750 UT in the sphere upstream. The magnetic field shear angle is 135° and the jump in amplitude is 1.25 from the sheath to sphere. The ion distribution functions (not shown) near the B_L reversal exhibit counterstreaming in V_N , and elongation in negative V_M , consistent with features of unmagnetized ions meandering near the current sheet midplane during reconnection [Wang *et al.*, 2016a, 2016b].

A zoom-in for the 3 s interval 011738.5–41.5 UT (marked by the blue horizontal bar in Figure 1a) is presented in Figures 1d–1h to highlight the following: (1) A strong electron flow (V_e in Figure 1e) of ~ 1300 km/s $\sim 7.2 V_A$ in M , yielding a current density $J_M \sim -1.5 \mu\text{A}/\text{m}^2$, and ~ 800 km/s $\sim 4.4 V_A$ in L , giving rise to $J_L \sim -1 \mu\text{A}/\text{m}^2$. (2) The electric field (Figure 1f) reverses sign in N and large-amplitude fluctuations (the data have been averaged to the electron measurement cadence of 30 ms/sample) in all three components begin upon entry into the exhaust (entry time will be discussed in Figure 2), causing in part fluctuations in V_e by $E \times B$ (similar to those observed in an electron jet event with a guide field $\sim 0.2 B_R$ [Khotyaintsev *et al.*, 2016]; further analysis of the wave fluctuations is left for future studies). (3) The energy dissipation due to the nonideal electric field $J \cdot E' = J \cdot (E + V_e \times B)$ (Figure 1g) as defined by Zenitani *et al.* [2011] increases to ~ 2 – 3 nW/m³ as V_{eM} climbs to its local maximum and remains positive until after B_L turns positive. (4) The electron temperatures $T_{e\parallel}$ and $T_{e\perp}$ (Figure 1h) both exhibit a trough correlated with V_{eM} due to traversal of the cold sheath inflow, as will be illustrated in Figure 2.

The electron distribution functions (DFs) observed during the concerted rises of V_{eM} , $J \cdot E'$ and $T_{e\perp}$ (DF center time is marked by the vertical dotted line in Figures 1d–1h) show signatures of the sheath part of the EDR. A DF example (Figure 1i) is presented in the magnetic field-aligned velocity coordinates in which

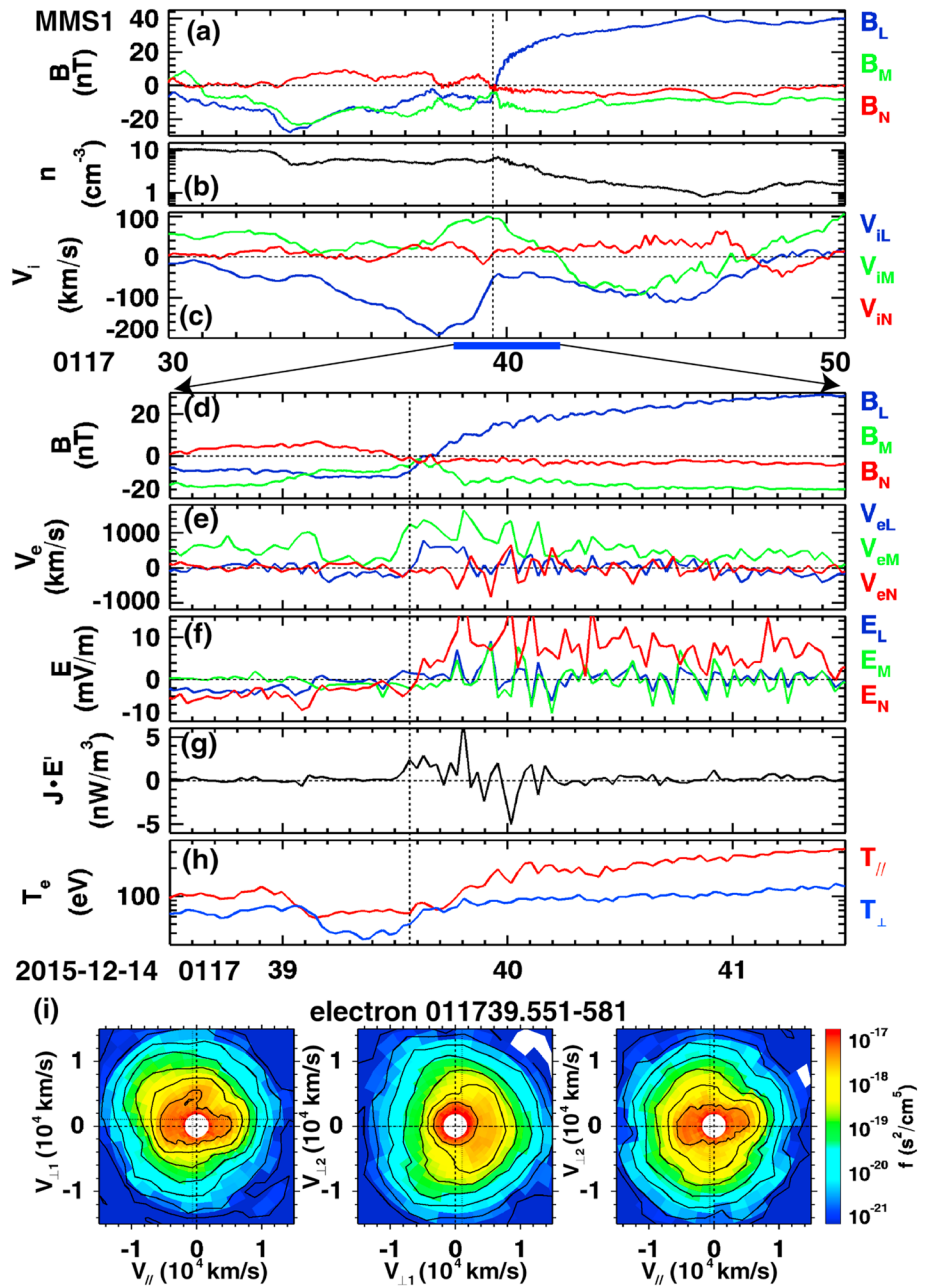


Figure 1. Overview of an EDR encounter by MMS. Data are from MMS1. (a) B in LMN with the transformation matrix to GSE given by $(L, M, N) = ([0.27, -0.54, 0.79], [-0.41, -0.82, -0.41], [0.87, -0.21, -0.44])$; (b) density n ; (c) the ion velocity V_{iLMN} ; (d–h) zoom-in view of B_{LMN} , V_{eLMN} , E_{LMN} (8192 samples/s averaged to the cadence of the electron data, 30 ms per sample), $J \cdot E'$ and $T_{e \parallel, \perp}$. (i) An electron distribution in three orthogonal velocity planes establishes that MMS1 encounters the sheath part of the EDR: a magnetic field-aligned counterstreaming sheath component combined with the EDR-accelerated electrons forming a triangular structure in $v_{\parallel} - v_{\perp 1}$. The nongyrotropic electrons are unmagnetized (see text for explanations) and contribute to a crescent-like shape in the v_{\perp} plane due to finite gyroradius effects.

$\hat{v}_{\perp 1} = (\hat{b} \times \hat{V}) \times \hat{b}$ and $\hat{v}_{\perp 2} = \hat{b} \times \hat{V}$ where \hat{b} and \hat{V} are the unit vectors of the magnetic field B and the electron velocity moment V_e , respectively. The component with $|v_{\perp 1}| < 3000$ km/s exhibits roughly balanced counterstreaming along B and a temperature anisotropy $T_{e \parallel} / T_{e \perp} \sim 2$ (Figure 1i, left), an anisotropy not displayed by ambient sheath electrons but predicted to be characteristic for the sheath inflow just upstream of the reconnection X line [Chen *et al.*, 2016a, 2016b]. The temperature anisotropy is likely a result of both acceleration by parallel electric fields over large scales in the ion diffusion region and perpendicular cooling due to

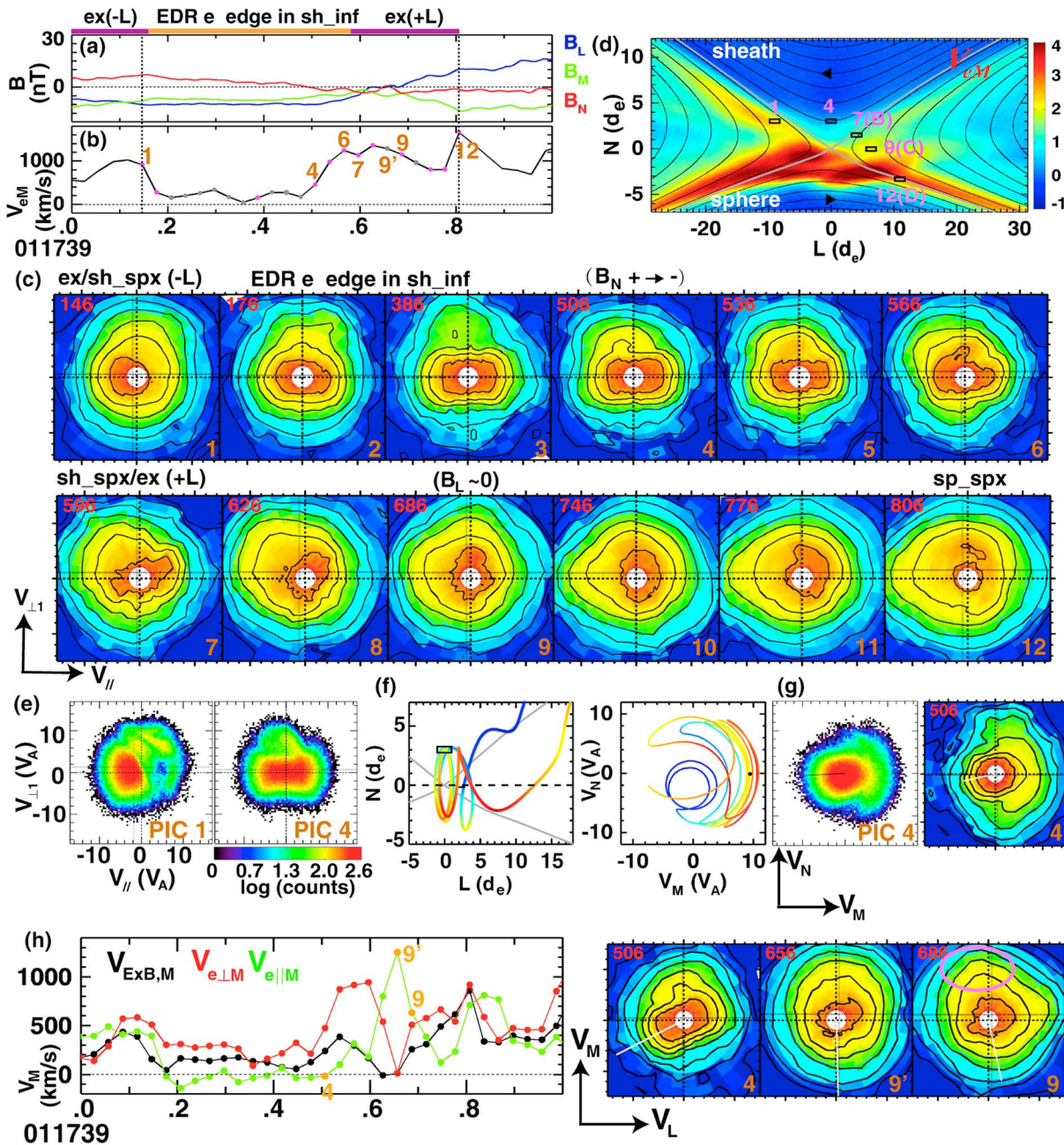


Figure 2. The distinct electron regions visited by MMS1 during its EDR encounter as revealed by the (c) DFs combined with (a) B and (b) V_{eM} , aided by PIC simulation results. Approximate locations of selected MMS1 DFs are plotted on the electron out-of-plane flow (d) V_{eM} from a PIC simulation to depict that MMS1 skims the sheath part of the V_{eM} edge and traverses the exhaust B_L reversal region. (e) The PIC DFs corresponding to MMS DFs 1 and 4. (f) An electron orbit in the $L-N$ plane (grey curves mark separatrices and color on the trajectory from cold to warm shows increasing $|v|$) and its corresponding crescent orbit in the $v_M - v_N$ ($\sim -v_L$) plane. (g) PIC DF 4 and MMS1 DF 4 in $v_M - v_N$ showing the crescent population (h) decomposition of V_{eM} and comparison with $V_{E \times B, M}$ along with $v_L - v_M$ DFs showing that the main contributors to V_{eM} vary with regions. The time in millisecond past 011739 UT is tagged in the upper left corner of each MMS1 DF panel to indicate the center time of the DF frame. Note that all MMS DFs (the ones without "PIC" labels) share the same colorbar and velocity range as those in Figure 1i.

conservation of the magnetic moment as incoming electrons travel to the weaker magnetic field region just upstream of the reconnection layer, similar processes as in symmetric magnetotail reconnection [Chen *et al.*, 2009; Egedal *et al.*, 2010].

The nongyrotropic component in Figure 1i consists of electrons that are more energetic than the sheath inflow population and exhibit a crescent-like structure in the $v_{L1} - v_{L2}$ plane (Figure 1i, middle), a signature of the finite gyroradius effects. When energized EDR electrons are captured near the turning points of their

gyroorbits (their accessible boundary in the sheath inflow), they exhibit the observed DF structure and mainly occupy the positive $v_{\perp 1}$ (roughly V_M at this time) half-plane. To see if these electrons cross the B_L reversal, the gyroradius R_g at $N_0/2$ is compared with the magnetic field gradient scale, where N_0 is the distance from the DF measurement location to $N = 0$ where $B_L = 0$. At $N_0/2$ the magnetic field is $B_{L0}/2$ in L and B_{M0} in M (the subscript 0 indicates the location $N = N_0$), assuming that B_L linearly decreases toward $B_L = 0$ and B_M remains constant. At the DF location, B_{LM} is $[-7.3, -4.7]$ nT (B_N is not relevant in this analysis as the gyration it causes has zero projection along N), averaged over the accumulation time (30 ms) of the DF. The magnetic field B_{LM} at $N_0/2$ is thus estimated to be $[-3.6, -4.7]$ nT which gives $R_g = 2.8$ km for electrons with $v_{\perp} = 3000$ km/s. The distance N_0 from the current sheet midplane is ~ 3.9 km ($\sim 2 d_e$) estimated by $V_N dt$, where $V_N \sim 30$ km/s is the spacecraft velocity in N determined by the timing of the four spacecraft B_L reversals and $dt = 0.13$ s is the difference between the DF (center) time to the MMS1 B_L reversal. The above estimates show that the measured electrons with $v_{\perp} > 3000$ km/s near the turning points of their gyroorbits have to cross $B_L = 0$ because $N_0/2 < R_g$. Note that $N_0/2$ is the magnetic gradient scale $B_L/(dB_L/dN)$ at $N_0/2$. The above criterion (the local gyroradius being larger than the magnetic gradient scale) has been employed to indicate demagnetization [Hesse *et al.*, 2016].

Another indication for electron demagnetization is based on the ratio between the magnetic curvature radius and the local thermal gyroradius, κ . A value of $\kappa^2 < 10$ is considered a sign of demagnetization [Büchner and Zelenyi, 1989; Lavraud *et al.*, 2016]. In the exhaust where $B_L \sim 0$, we have $\kappa^2 \sim 3$ (or 2.5 ± 1.6 , where the error is due to the spacecraft separation being about 4 times the radius of curvature and estimated based on the error determination given in Shen *et al.* [2003]), supporting that the electrons are not magnetized as they enter the vicinity of the current sheet midplane. The magnetic curvature used for the κ calculation is obtained using the Magnetic Curvature Analysis with the magnetic field data from the four spacecraft [Shen *et al.*, 2003; Lavraud *et al.*, 2016]. We emphasize that the method of comparing the gyroradius and the magnetic gradient scale as well as the κ estimate independently indicates electron demagnetization, even though the methods do involve uncertainties in the structure velocity determination and magnetic curvature calculation, respectively.

In the vicinity of the B_N reversal, the type of nongyrotropic DF discussed above is predicted by PIC simulations to exist only within a few d_e from the B_L reversal in the sheath part of the EDR for magnetopause reconnection (Figure 3i shows that no crescent population at $v_{\perp 1} > 0$ at $N \sim 4 d_e$ from the B_L reversal.). The $v_{\parallel} - v_{\perp 2}$ DF in Figure 1i shows an elongation along $v_{\perp 2}$ (right), a feature also observed in a previously reported EDR event [Chen *et al.*, 2016b].

The distinct electron regions traversed by MMS1 during the interval marked by the vertical dotted lines on the B and V_{eM} profiles (Figures 2a and 2b) are “imaged” with the DFs in $v_{\parallel} - v_{\perp 1}$ (Figure 2c, same colorbar as that in Figure 1i). The shown frames are indexed with numbers displayed in the lower right corner of each DF panel, and their corresponding time points are marked with pink dots in Figure 2b (a number of frames are omitted due to similarities to their neighboring frames, and their corresponding data points are colored grey).

In DF 1, the incoming sheath electrons only appear with $v_{\parallel} < 0$, and together with the observed $B_L < 0$ and $B_N > 0$ indicate a location on reconnected field lines (exhaust) in the $-L$ side of the X line. Hence, the annotation “ex/sh_spx(-L)” to inform that DF 1 is the last frame in the exhaust before entering the not-yet-reconnected flux tubes in the sheath. DF 2 has two components: (1) a sheath population balanced in $v_{\parallel} < 0$ and $v_{\parallel} > 0$ with $T_{e\parallel}/T_{e\perp} \sim 2$, predicted sheath inflow T_e anisotropy just upstream of the EDR (see Figure 3i), and (2) an approximately “triangle-shaped” population with $v_{\perp 1} > 0$. The triangle population is interpreted as due to subgyroscale sampling of the accelerated meandering EDR electrons at their accessible boundary (EDR e edge). The two components together imply a location on not-yet-reconnected sheath field lines (sheath inflow) at the EDR electron edge and hence denoted as “EDR e-edge in sh_inf.” DFs 2–6 (and those marked with grey in the interval .2–.5 s in Figure 2b) all belong to the same region with slightly varying depths into the EDR: the deeper into the EDR, the more meandering electrons are present, and thus the higher the phase-space-density (PSD) of the triangular component (such as DF 2 and DFs 4–6). Note that the triangular component in $v_{\parallel} - v_{\perp 1}$ corresponds to a crescent-like structure in $v_{\perp 1} - v_{\perp 2}$, similar to that shown in Figure 1i. The crescent orbits responsible for the crescent-like DF structure will be illustrated in Figure 2f.

The MMS1 crossing of the separatrix from the sheath inflow occurs at the time of DF 7 in which the high-PSD (orange color) sheath electrons with $v_{\parallel} < 0$ have largely disappeared. In DF 8, the sheath remnant (identified by the high PSD) electrons are no longer magnetized by the local B . During the interval covering DFs 9–10, the sheath remnants are elongated along $v_{\perp 1}$ and their $v_{\perp 1}$ thermal width is larger than that in the sheath inflow (DFs 2–6), indicating that these electrons are demagnetized. At DF 10, the perpendicularly elongated sheath remnant is biased toward $v_{\parallel} > 0$ and shifted to $v_{\parallel} > 0$ in DF 11. In DFs 9–12 at $B_L > 0$, the field-aligned electrons at $v_{\parallel} < 0$ are likely the sphere inflow population traveling toward the X line. In DFs 7–9 where $B_L \leq 0$, the non-gyrotropic electrons may be accelerated meandering electrons that originate from sheath and/or sphere.

The approximate MMS1 locations corresponding to selected DFs are plotted on V_{eM} (Figure 2d) from a PIC run (with the same simulation parameters as those in *Chen et al.* [2016a], except for a uniform guide field $0.2 B_R$ along the direction of the reconnection current and an increased average number of particles per cell to 6000. See Appendix A for a summary of the simulation setup). The V_{eM} in the PIC run indicates that the region of enhanced V_{eM} extends to the sheath inflow region within a few d_e in N from the B_L reversal. The DF locations are inferred based on the measured B_{LMN} , V_{eM} , and the 12 DFs, aided by the simultaneous four spacecraft measurements. For example, the time of DF 12 is when MMS1 encounters the sphere separatrix (labeled as DF1D in the DF array in Figure 3i) and MMS4 registers the sheath separatrix.

The PIC DFs corresponding to MMS DFs 1 and 4 (taken from locations 1 and 4 indicated in Figure 2d) are presented in Figure 2e to illustrate the MMS-PIC comparison and to further support the interpretations of the MMS data so far. PIC DF 1 from the exhaust ($-L$ side of the X line) near the separatrix shows the incoming sheath population with $v_{\parallel} < 0$, and a slight nongyrotropy with higher PSD at $v_{\perp 1} > 0$, similar to the MMS1 DF 1 features. PIC DF 4 is from the sheath edge of the current layer at $L \sim 0$, and in addition to the sheath inflow population with $T_{e\parallel} > T_{e\perp}$ exhibits finite gyroradius signatures of the meandering EDR electrons at $v_{\perp 1} > 0$, resembling MMS1 DF 4.

How do electrons meander in a guide-field reconnection configuration? To illustrate this, an electron orbit in the L - N plane (rainbow colors to show $|v|$ variations) and its corresponding crescent orbit in $v_M - v_N$ are plotted as an example (Figure 2f). The test electron is taken from the tip of PIC DF 4 (Figure 2e; see Figure 2d for the L - N location of DF 4) with $v_{\parallel} = -2.5$, $v_{\perp 1} = 7.5$ for both forward and backward tracing in time for $0.27 \omega_{ci}^{-1}$ and $0.65 \omega_{ci}^{-1}$, respectively. The electron originates from the sheath, travels toward $-L$ and bounces in the EDR, gains momentum (shown as the color change from cold to warm along the trajectory) due to acceleration by the reconnection electric field ($E_M < 0$, measured by MMS and will be shown in Figures 3f and 3f'), and finally is ejected into the exhaust. The effect of the guide field is seen as the looping back in L , that is, sign reversals of v_L due to its gyration around B_M . The meaning of "meandering" (used to describe the particle bounce motion at the field reversal region of a current sheet with zero guide field [*Speiser*, 1965; *Horiuchi and Sato*, 1994]) is generalized here to include the motion around B_M . The orbit as a hybrid produced by the Larmor and bounce motion exhibits a crescent shape in the $v_M - v_N$ plane (approximately the plane perpendicular to B). The turning points at maximum $|v_M|$ of the crescent orbits are shifted toward $+v_M$ due to acceleration by E_M as the electron bounces at the B_L reversal. In contrast, the turning points at maximum $|v_N|$ of the crescent orbits analyzed by *Bessho et al.* [2016] do not shift, since E_M is not included and E_N being electrostatic cannot produce a net acceleration (shift in v_M) when the particles bounce back to the region with the same E_N . The electrons in the crescent population of the $v_M - v_N$ DF (labeled PIC4 in Figure 2g) are captured near the electron edge of the sheath EDR at the location marked with a black rectangle in the L - N orbit panel (marked by a black box labeled "4" in Figure 2d) and compare favorably with the MMS DF 4 in $v_M - v_N$ (Figure 2g). These crescent-shaped DFs are qualitatively similar to those observed in the negligible guide-field cases [*Burch et al.*, 2016; *Chen et al.*, 2016b], since the crescent-shaped nongyrotropy is a generic consequence of resolving subgyroradius scales at a plasma boundary. Specific quantitative differences between crescent DFs due to effects of E_M and the guide field will be reported elsewhere.

After surveying the landscape of the EDR traversed by MMS1, we are now ready to examine the makeup of the reconnection current, which is mainly due to the electron out-of-plane flow V_{eM} (the out-of-plane current density $J_M = ne (V_{iM} - V_{eM}) \sim -neV_{eM}$ and its time profile are nearly identical to that of V_{eM}). In Figure 2h, the M components of $V_{e\parallel}$ and $V_{e\perp}$ are presented (based on the decomposition: $V_{eM} = V_e \cdot \hat{M} = (V_{e\parallel} + V_{e\perp}) \cdot \hat{M} = V_{e\parallel M} + V_{e\perp M}$) to show that the reconnection current is due to a combination of perpendicular and

parallel electron flows once in the exhaust (~ 011739.61 – 011739.81 UT), while predominantly by the perpendicular flow at the EDR electron edge in the sheath inflow (data points lying under the horizontal orange bar above Figure 2a). The M component of $V_{E \times B}$ is overplotted to show that $V_{e \perp M}$ deviates from $V_{E \times B, M}$ until just before 011739.8 UT when MMS1 approaches the sphere separatrix.

The $v_L - v_M$ DF panels in Figure 2h (corresponding data points are colored orange on the $V_{e \parallel M}$ trace) provide insight into the kinetic meaning of the flow decomposition. The meandering electrons are the key contributors to V_{eM} at the EDR electron edge in the sheath inflow (DFs 2–6 with DF 4 shown in $v_L - v_M$ as an example illustrating the common feature), and the velocities of these electrons are primarily perpendicular to B (the white line represents the projection of B onto the $v_L - v_M$ plane, and the line length H satisfies $\sqrt{(B_L^2 + B_M^2)}/B = H/v_r$, where v_r is the velocity range of the DF plot, $1.5e4$). From the sheath separatrix to the current sheet midplane (DFs 7, 8, and 9'), the demagnetized/meandering electrons are still the main carriers of V_{eM} , and the increasing $V_{e \parallel M}$ is primarily due to the rotation of the local magnetic field to nearly $-\hat{M}$ (see B_{LMN} in Figure 2a). The meandering population exhibits nongyrotropy in DFs 7 and 8 (Figure 2c) and occupies the $v_M > 0$ half-plane (not shown) in a manner similar to that in DF 9'. The much larger v_\perp thermal spread of the high v_M (> 6000 km/s) electrons in DF 9' (Figure 2h) than in DF 9 suggests demagnetization to change pitch angles of the inflowing field-aligned sphere electrons (the population with large positive v_M inside the magenta circle in DF 9 in Figure 2h). Furthermore, as discussed in Figure 1i, κ^2 is approximately 3 at the current sheet midplane from which DF 9' is taken, supporting that DF 9' contain demagnetized electrons. Note that in DF 9', the finite bulk $V_{e \perp}$ is in the $+L$ direction with negligible projection onto \hat{M} .

On the sphere side of the current sheet midplane (DFs 9–12 illustrated with DF 9 as an example shown in Figure 2h) to the sphere separatrix, V_{eM} is carried by a mixture of inflowing field-aligned sphere electrons (the population with large positive $v_\parallel < 0$ inside the magenta circle in DF 9, and the population at $v_\parallel < 0$ in DFs 10–12 in Figure 2c) and meandering electrons. The meandering population is manifested in DF 9 (Figure 2h) as the component at $v_L > 0$. For DFs 10–12, applying the same analysis as that for Figure 1i, the local gyroradius of electrons with $v_\perp \sim 6000$ km/s at $[B_L/2, B_M]$ is ~ 4.1 km, 3.2 km, and 2.3 km, respectively, and they are all larger than or comparable with the estimated $N/2$ at each DF location (1.4 km, 1.8 km, and 2.2 km for DFs 10–12, respectively, based on the spacecraft velocity $V_N \sim 30$ km/s). Hence, the electrons with $v_\perp > 6000$ km/s in DFs 10–12 are considered demagnetized/meandering.

The EDR encounter of MMS1 is now placed in the four-spacecraft perspective (Figure 3). The density in the exhaust and sheath inflow (at 01:17:39.55 UT, for example) is approximately 6 cm^{-3} , yielding an electron skin depth ($1 d_e = 1 c/\omega_{pe}$) ~ 2 km. MMS1 is the closest to the Earth (smallest N) and separated from the other three spacecraft by ~ 12 – 15 km (~ 6 – $7.5 d_e$) in N (Figure 3a). Such placement in N combined with the widening of the distance between the two sheath separatrices toward increasing N results in the shortest sheath inflow traversal time of MMS1 compared with the other spacecraft as evidenced by their V_{eM} profiles (Figure 3e). MMS2–MMS4 though separated in L and M by ~ 5 – $7 d_e$ are close to one another in N , and their B_L values are nearly identical until 011739.7 UT when MMS3–2–4 entered the electron-scale current sheet in the order of increasing N coordinate values.

The approximately constant B_L (Figure 3b) during the sheath inflow crossing indicates that the normal velocity of the spacecraft relative to the reconnection layer is ~ 0 . All four MMS detect a B_N reversal from positive to negative (Figure 3d), further supporting the picture that the spacecraft moves from $-L$ side to $+L$ of the X line as inferred from the DFs in Figure 2.

One effect of the finite guide field is to modify the exhaust B_M structure. The modification predicted by the PIC simulation is that a guide-field-dominated region is created between the in-plane X line and the asymmetric Hall B_M pattern (Figure 3j). As MMS1 enters the sheath separatrix (frame B marked by the vertical line at 011719.6 UT in Figure 3c and indicated in Figure 3j) into the exhaust and onward to the sphere separatrix (frame D marked in Figures 3c, 3i, and 3j), its B_M remains negative, evidence for the guide-field-dominated region. A brief excursion to positive B_M (and $B_L < 0$) is observed by MMS2–MMS4 at ~ 011739.7 – $.8$ UT, indicating traversal through the Hall B_M which is positive near the sheath separatrix. The B_M variations observed by the four MMS spacecraft are consistent with the PIC B_M structure and the spacecraft relative positions. The guide-field-dominated region is constrained to be of the d_e scale and its width in N is smaller than $7.5 d_e$.

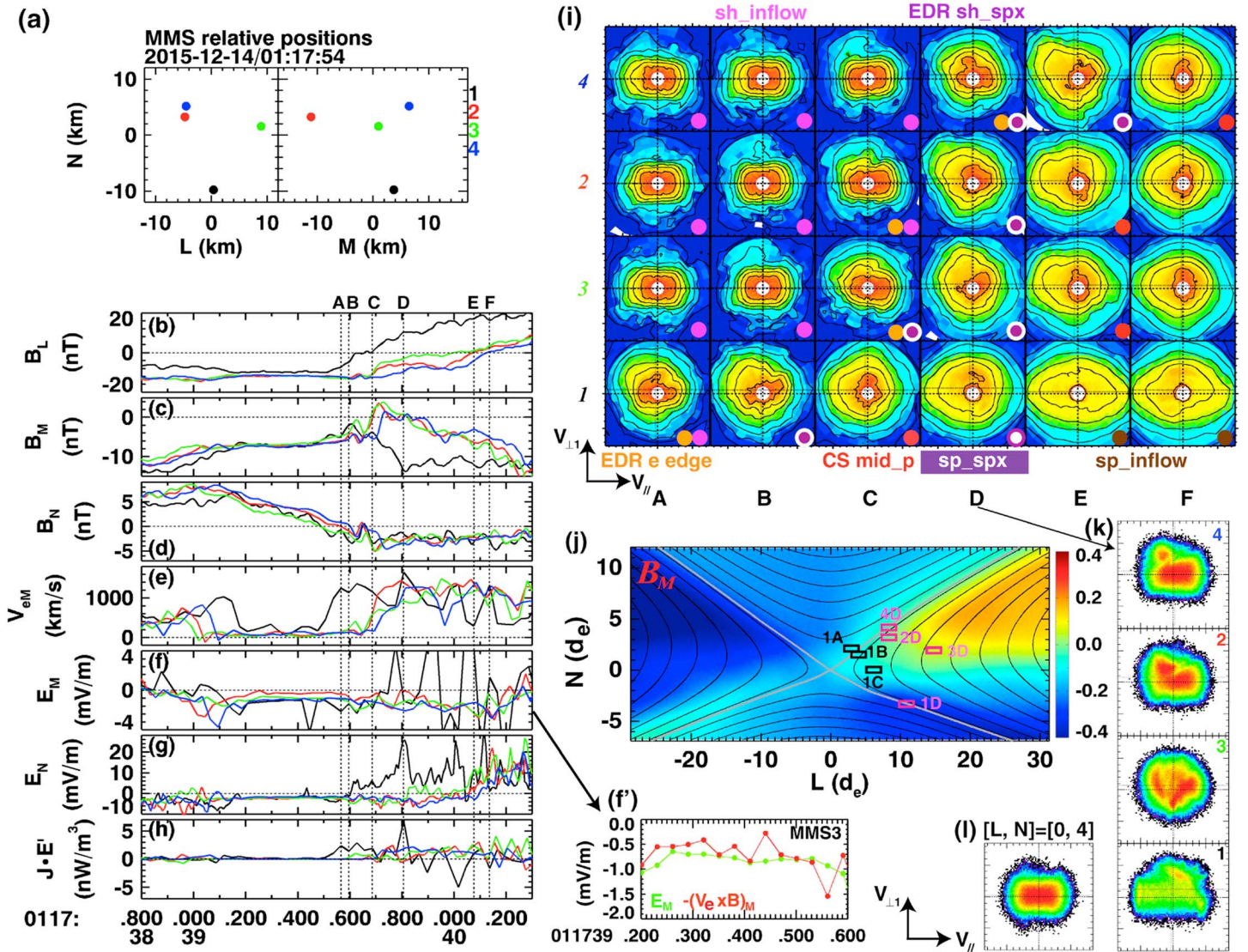


Figure 3. The EDR encounter by the four MMS spacecraft and comparison with PIC simulation results. (a) Relative positions of the spacecraft. (b) B_L and (c) B_M at MMS1 remain negative even in the sheath part of the $+L$ exhaust, indicating a guide-field dominated region. MMS2–MMS4 observe a brief positive B_M excursion, showing traversals of the edge of the Hall B-dominated region. (d) The B_N reversals of all four spacecraft imply a transition from $-L$ to $+L$ of the X line. (e) The electron out-of-plane flow V_{eM} . (f) The out-of-plane electric field E_M , consistent with the expected reconnection electric field. (g) Agreement of the MMS3 E_M and $-(V_e \times B)_M$, supporting the accuracy of EM measurements in the sheath inflow. (h) The electric field normal to the current layer E_N (averaged to the cadence of the B data, 128 sample/s) reverses sign slightly before the B_L reversal for each spacecraft (h) The energy conversion due to the nonideal E ($J \cdot E'$) enhances with V_{eM} . (i) MMS $v_{||} - v_{\perp 1}$ DF array (using the same colorbar and velocity range as those in Figure 1i) arranged according to the N positions of the spacecraft in rows and time in columns (A–F from left to right, corresponding to the vertical dotted lines marked in Figures 3b–3h) to provide a visual for the EDR encounter. The distinct electron regions are color coded and annotated. (j) PIC simulation predictions for B_M . (k) The PIC DFs for the four spacecraft locations at frame D (the spacecraft locations are marked by magenta boxes in Figure 3j). For reference, the locations of MMS1 for frames A–C are also noted (black) in the B_M panel to facilitate the comparison with the DFs in Figure 2. (l) A PIC DF showing that only sheath inflow electrons are present at $N > -4 d_e$ from $B_L = 0$.

based on the combined facts that MMS1 crosses the region with $B_M < 0$ and $B_L < 0$ and MMS2–MMS4 encounter the region of $B_M > 0$ and $B_L < 0$ before the time of frame D when the distance between the sheath and sphere separatrices is inferred to be $\sim 7.5 d_e$ (see the discussion for DF frame D).

The observed E_M direction and amplitude agree with the PIC prediction for the reconnection electric field. For all spacecraft, E_M (Figure 3f) stays at steady values of approximately -0.3 to -1 mV/m during the interval 011739.2–.5 UT when B_L is virtually constant in the sheath inflow. The E_M values measured by MMS1, MMS3, and MMS4 are nearly identical, consistent with the uniform E_M over d_i scale in PIC simulations [e.g., Hesse et al., 2014, 2016]. The only exception is the departure between 011739.4 and 011739.5 UT due to a

double-layer-like structure (similar to those reported in prior studies [Fujimoto, 2014; Chen et al., 2015; Ergun et al., 2016b]) registered by MMS1 (based on the burst data, not shown). To further substantiate the E_M measurement accuracy, note that MMS3 is outside of the EDR in the sheath inflow, detecting an average $E_M \sim -0.84$ mV/m (Figure 3f) and $-(V_e \times B)_M \sim -0.71$ mV/m. For the PIC run with the same MMS guide field, at approximately the peak reconnection rate, $E_M \sim 0.125 V_A B_R$ (where V_A is the Alfvén speed based on the upstream sheath density and $|B_L| \sim -0.47$ mV/m if using $n = 6 \text{ cm}^{-3}$ and $B_L = -20$ nT (from ~ 011735 UT), and -1.22 mV/m if using $n = 8 \text{ cm}^{-3}$ and $B_L = -30$ nT (from ~ 012030 UT).

The normal electric field E_N (Figure 3g) switches sign to positive slightly earlier than the B_L positive turning, consistent with the PIC simulation prediction that the positive E_N region extends slightly to the sheath side of the B_L reversal (not shown for the $B_g = 0.2$ run reported in this paper but similar to the $B_g = 0$ case shown in Chen et al. [2016a]); $J \cdot E'$ picks up at the time when V_{eM} increases, remains primarily positive until after B_L turns positive, and displays significant variations subsequently. Accelerated meandering electrons have been shown to be responsible for the V_{eM} increase (Figure 2), and thus the concerted rises of V_{eM} and $J \cdot E'$ support that the demagnetization of electrons in the reconnection current layer contributes to the energy dissipation due to the nonideal electric field. Wave fluctuations may provide additional contribution and lead to $J \cdot E'$ variations.

The EDR is visualized in the $v_{\parallel} - v_{\perp 1}$ DF array measured by the four MMS (Figure 3i). The $v_{\parallel} - v_{\perp 1}$ DFs best show the magnetized sheath electrons counterstreaming along B and the EDR electrons at $v_{\perp 1} > 0$. The asymmetry with respect to $v_{\perp 1} = 0$ cannot be removed by any Galilean transformation and indicates nongyrotropy. The selected frames A–F are discussed below. Note that frames A–D for MMS1 correspond to DF 6, DF 7, DF 9, and DF 12 in Figure 2 (and hence discussions on these DFs will not be repeated here) and are shown in Figure 3i to provide a basis for interpreting the four-spacecraft DFs.

- A: MMS2–MMS4 are in the sheath inflow observing only the anisotropic sheath electrons that have been accelerated parallel to B and no EDR electrons. These sheath inflow DFs correspond to the PIC DF h1 in Figure 1 of Chen et al. [2016a], and their characteristics do not change appreciably even with a guide field of 0.2, as confirmed by the DF in Figure 3i. Here the DFs from the four spacecraft enable us to visualize how the meandering population at $v_{\perp 1} > 0$, which is the crescent population in $v_{\perp 1} - v_{\perp 2}$, may contribute to the inertial term to balance E_M : V_{eM} increases toward decreasing N , together with $V_{eN} < 0$ (Figure 1e) observed by MMS1, yielding a finite $V_{eN} \cdot \partial V_{eM} / \partial N$.
- B: MMS2–MMS4 are still in the sheath inflow with MMS2 and MMS3 approaching the accessible edge of the EDR electrons, as hinted by the faint enhancement of the non-gyrotropic population at $v_{\perp 1} > 0$.
- C: MMS2 and MMS3 are in the sheath separatrix vicinity, and MMS4 approaches the EDR electron edge in the sheath inflow.
- D: MMS2 and MMS3 cross the sheath separatrix region, losing antiparallel ($v_{\parallel} < 0$) sheath electrons, similar to the MMS1 DF in frame B. For MMS4, the field-aligned sheath electrons with $v_{\parallel} < 0$ are diminishing, while accelerated sheath electrons appeared in $v_{\perp 1} > 0$ with low-parallel speeds, indicating the separatrix crossing in the sheath part of the EDR. The sphere and sheath separatrices are inferred to be $\sim 7.5 d_e$ apart, based on the DFs registered by MMS1 and MMS4.
- E: MMS1 observes the sphere inflow, outside of the separatrix, as indicated by the counterstreaming sphere inflow electrons and no discernable sheath electrons; MMS2 and MMS3 are at the B_L reversal in the exhaust, while MMS4 detects the exhaust side of the sheath separatrix before reaching the B_L reversal, corresponding to the MMS1 DF in frame B. Both MMS2 and MMS3 register meandering sheath electrons with $v_{\parallel} \sim 0$, and at $v_{\parallel} < 0$, a mixture of incoming sphere and meandering electrons.
- F: MMS1 in the sphere inflow with $T_{e\parallel} > T_{e\perp}$, while MMS4 in the exhaust where $B_L \sim 0$. MMS2 and MMS3 are near the current sheet midplane on the sphere side with the unmagnetized sheath population slightly shifted toward $v_{\parallel} > 0$, a feature also seen in DF 10 in Figure 2c.

The above DF array demonstrates that all four spacecraft encounter the EDR, as they all register the meandering sheath and sphere electrons in the sheath inflow, sheath separatrix, and the current sheet midplane where B_L vanishes. The interpretations of the MMS data are further strengthened by PIC simulation results. The PIC B_M (Figure 3j) shows that the asymmetric quadrupolar Hall magnetic field dominates much of the exhaust. To the right (+L) of the in-plane null, only a d_e -scale region of $B_M < 0$ can be found in the exhaust with $B_L < 0$, and it is encountered by MMS1. The PIC predictions for MMS DF frame D (Figure 3k) support

the validity to place MMS4 at the sheath separatrix and MMS1 at the sphere separatrix, and the PIC-MMS agreement suggests that the 2-D reconnection configuration is not far from the reality for the reported event. The PIC DFs corresponding to MMS2 and MMS3 locations also present reasonable agreement with the observed DFs. To constrain the N width of the EDR electron edge in the sheath inflow, a PIC DF from $[L, N] = [0, 4] d_e$ is plotted to show that no EDR electrons can be discerned at $N > \sim 4 d_e$ away from $B_L = 0$ (at $N \sim 0$) and the T_e anisotropy of the sheath inflow is comparable to that measured by MMS2–MMS4 in frame A, for example.

4. Summary and Conclusions

In summary, an EDR during magnetopause reconnection with a weak but not negligible guide field ($0.2 B_R$) is visualized with electron distribution functions from all four MMS spacecraft, and the questions regarding the reconnection current, reconnection rate, and effects of the guide field are addressed. The observed nongyrotropic DFs along with the estimated magnetic scale indicates that the majority of electrons are demagnetized inside the EDR, as the gyroradii of the nongyrotropic electrons are comparable or larger than the inferred magnetic scale length. Motion of the demagnetized electrons (bouncing at the field reversal, gyrating around the weak guide field, and accelerating by the reconnection electric field as illustrated in Figure 2) plays an important role to sustain the reconnection current and contributes to the dissipation due to the non-ideal electric field ($J \cdot E$). The inflowing field-aligned magnetosphere electrons are demonstrated to be also important in carrying the reconnection current in the magnetosphere part of the EDR where the reconnecting magnetic field B_L is positive. In the EDR, the inflowing field-aligned electrons are demagnetized at the midplane of the current sheet due to the large magnetic curvature and gradient, and their bouncing orbit widths allow them to reach and even go beyond the separatrices. The presence of unmagnetized electrons on not-yet-reconnected field lines (the magnetosheath or magnetosphere inflow) is an important feature of the EDR.

The guide field modifies the out-of-plane magnetic field B_M structure in the exhaust. A d_e -scale region where the guide field dominates over the Hall magnetic field is encountered (by MMS1) and shown (by data from MMS2 to MMS4) to be followed by an asymmetric Hall B_M pattern on the downstream side. As a consequence of the competition between the guide field and the Hall field in the exhaust observed by MMS, the magnetic field near the midplane is weak and electrons in the EDR may be demagnetized more easily at the midplane than the case with zero guide field in which the exhaust is dominated by a nearly unipolar Hall B_M [Pritchett, 2008; Norgren *et al.*, 2016], a counter-intuitive result for the intermediate guide-field regime. On the other hand, the guide field may allow the inflowing field-aligned sphere electrons to penetrate deeper and reach nearly the current sheet midplane, as the B_M reversal is now pushed downstream and to the magnetosheath side of the EDR, in comparison with the zero guide-field case (see Norgren *et al.* [2016] for a zoom-in view of the B_M structure in zero-guide field asymmetric reconnection).

The four-spacecraft observations of the magnetosheath inflow, including the EDR electron edge, offer a firm ground to determine the reconnection electric field E_R . E_R is shown to be uniform over at least the interspacecraft ($\sim 8 d_e$) and corresponds to a reconnection rate ~ 0.1 . The spacecraft upstream of the EDR provides independent checks on E_R based on $-V_e \times B$.

In conclusion, the MMS four-spacecraft measurements establish the first observation-based picture of an EDR in magnetopause reconnection under an intermediate guide field. The guide field is not strong enough to destroy the meandering orbit dynamics but does create a new out-of-plane magnetic field structure which in turn introduces new electron flow dynamics in the magnetosphere side of the EDR.

Appendix A

The simulation presented here starts with an ion-scale current sheet with a uniform guide field and ratios of the upstream densities $n_0/n_1 = 8$ and magnetic fields $B_0/B_1 = 1.37$ between the magnetosheath (high density) and magnetosphere (low density). The initial magnetic field is $B(N) = [(B_1 - B_0)/2 - (B_1 + B_0)/2 \cdot \tanh(N/\lambda)] \hat{L} - 0.2 B_0 \hat{M}$, where $\lambda = 1 d_i$ (ion skin depth based on n_0) and B_0 are the same as B_R in the main text. A sinusoidal perturbation is applied to seed a reversal in B_N to initiate reconnection [Daughton *et al.*, 2006]. The density

profile is $n(N) = n_h(N) + n_b(N)$, where the Harris density $n_h(N) = n_c / \cosh^2(N/\lambda)$ with n_c the density at the layer center and $n_b(N) = (n_1 + n_0)/2 + (n_0 - n_1)/2 \cdot \tanh(N/\lambda)$. Pressure balance is satisfied with $[(B_1 + B_0)/2]^2 = 2\mu_0 n_c (T_i + T_e)$ and $B_1^2 - B_0^2 = 2\mu_0 (n_0 - n_1)(T_i + T_e)$, where $T_{i,e}$ are uniform initial temperatures for ions and electrons, respectively. The domain has $75 \times 25 d_i$ resolved by 3072×2048 cells. Other parameters are as follows: ratio of the sheath electron plasma and cyclotron frequencies $\omega_{pe}/\omega_{ce} = 2$, mass ratio $m_i/m_e = 100$, temperature ratio $T_i/T_e = 2$, and $\beta_{0,1} = 2\mu_0 n_{0,1}(T_i + T_e)/B_{0,1}^2 = 1$ (sheath), 0.067 (sphere). The boundary conditions are periodic in L while reflecting for particles and conducting for fields in N . The average number of particles per cell is 6000. In the paper, velocities are in units of V_A based on B_0 and n_0 , and lengths in d_e using n_0 .

Acknowledgments

The research was supported in part by the NASA Magnetospheric Multiscale mission and by DOE grant DESC0016278, and NSF grants AGS-1202537, AGS-1543598, and AGS-1552142. The simulation run was performed on Pleiades under the NASA High-End Computing Program through the NASA Advanced Supercomputing Division at Ames Research Center. The MMS data are available at the MMS Science Data Center, and PIC data are available upon request to the authors.

References

- Bessho, N., L.-J. Chen, and M. Hesse (2016), Electron distribution functions in the diffusion region of asymmetric magnetic reconnection, *Geophys. Res. Lett.*, *43*, 1828–1836, doi:10.1002/2016GL067886.
- Burch, J. L., T. Moore, R. Torbert, and B. Giles (2015), Magnetospheric multiscale overview and science objectives, *Space Sci. Rev.*, *199*, 5–21, doi:10.1007/s11214-015-0164-9.
- Burch, J. L., et al. (2016), Electron-scale measurements of magnetic reconnection in space, *Science*, *352*(6290), 1189, doi:10.1126/science.aaf2939.
- Burch, J. L., and T. D. Phan (2016), Magnetic reconnection at the dayside magnetopause: Advances with MMS, *Geophys. Res. Lett.*, *43*, 8327–8338, doi:10.1002/2016GL069787.
- Büchner, J., and L. M. Zelenyi (1989), Regular and chaotic charged particle motion in magnetotail-like field reversals: 1. Basic theory of trapped motion, *J. Geophys. Res.*, *94*(A9), 11,821–11,842, doi:10.1029/JA094iA09p11821.
- Chen, L.-J., et al. (2009), Multispacecraft observations of the electron current sheet, neighboring magnetic islands, and electron acceleration during magnetotail reconnection, *Phys. Plasmas*, *16*, 056501, doi:10.1063/1.3112744.
- Chen, L.-J., M. Hesse, S. Wang, N. Bessho, and W. Daughton (2016a), Electron energization and structure of the diffusion region during asymmetric reconnection, *Geophys. Res. Lett.*, *43*, 2405–2412, doi:10.1002/2016GL068243.
- Chen, L.-J., et al. (2016b), Electron energization and mixing observed by MMS in the vicinity of an electron diffusion region during magnetopause reconnection, *Geophys. Res. Lett.*, *43*, 6036–6043, doi:10.1002/2016GL069215.
- Chen, Y., K. Fujimoto, C. Xiao, and H. Ji (2015), Plasma waves around separatrix in collisionless magnetic reconnection with weak guide field, *J. Geophys. Res. Space Physics*, *120*, 6309–6319, doi:10.1002/2015JA021267.
- Daughton, W., J. Scudder, and H. Karimabadi (2006), Fully kinetic simulations of undriven magnetic reconnection with open boundary conditions, *Phys. Plasmas*, *13*, 072101, doi:10.1063/1.2218817.
- Denton, R. E., B. U. Ö. Sonnerup, H. Hasegawa, T. D. Phan, C. T. Russell, R. J. Strangeway, B. L. Giles, D. Gershman, and R. B. Torbert (2016), Motion of the MMS spacecraft relative to the magnetic reconnection structure observed on 16 October 2015 at 1307 UT, *Geophys. Res. Lett.*, *43*, 5589–5596, doi:10.1002/2016GL069214.
- Egedal, J., A. Lê, N. Katz, L.-J. Chen, B. Lefebvre, W. Daughton, and A. Fazakerley (2010), Cluster observations of bidirectional beams caused by electron trapping during antiparallel reconnection, *J. Geophys. Res.*, *115*, A03214, doi:10.1029/2009JA014650.
- Eriksson, S., et al. (2016), Magnetospheric multiscale observations of the electron diffusion region of large guide field magnetic reconnection, *Phys. Rev. Lett.*, *117*, 015001, doi:10.1103/PhysRevLett.117.015001.
- Ergun, R., et al. (2016a), The axial double probe and fields signal processing for the MMS mission, *Space Sci. Rev.*, *199*(1–4), 167–188, doi:10.1007/s11214-014-0115-x.
- Ergun, R. E., et al. (2016b), Magnetospheric multiscale observations of large-amplitude, parallel, electrostatic waves associated with magnetic reconnection at the magnetopause, *Geophys. Res. Lett.*, *43*, 5626–5634, doi:10.1002/2016GL068992.
- Fujimoto, K. (2014), Wave activities in separatrix regions of magnetic reconnection, *Geophys. Res. Lett.*, *41*, 2721–2728, doi:10.1002/2014GL059893.
- Fujimoto, K., and R. D. Sydora (2009), Particle description of the electron diffusion region in collisionless magnetic reconnection, *Phys. Plasmas*, *16*(11), 112–309, doi:10.1063/1.3263694.
- Hesse, M., T. Neukirch, K. Schindler, M. Kuznetsova, and S. Zenitani (2011), The diffusion region in collisionless magnetic reconnection, *Space Sci. Rev.*, *160*, 3–23.
- Hesse, M., N. Aunai, S. Zenitani, M. Kuznetsova, and J. Birn (2013), Aspects of collisionless reconnection in asymmetric systems, *Phys. Plasmas*, *20*, 061210.
- Hesse, M., N. Aunai, D. Sibeck, and J. Birn (2014), On the electron diffusion region in planar, asymmetric, systems, *Geophys. Res. Lett.*, *41*, 8673–8680, doi:10.1002/2014GL061586.
- Hesse, M., Y.-H. Liu, L.-J. Chen, N. Bessho, M. Kuznetsova, J. Birn, and J. L. Burch (2016), On the electron diffusion region in asymmetric reconnection with a guide magnetic field, *Geophys. Res. Lett.*, *43*, 2359–2364, doi:10.1002/2016GL068373.
- Horiuchi, R., and T. Sato (1994), Particle simulation study of driven magnetic reconnection in a collisionless plasma, *Phys. Plasmas*, *1*, 3587, doi:10.1063/1.870894.
- Khotyaintsev, Y. V., et al. (2016), Electron jet of asymmetric reconnection, *Geophys. Res. Lett.*, *43*, 5571–5580, doi:10.1002/2016GL069064.
- Lavraud, B., et al. (2016), Currents and associated electron scattering and bouncing near the diffusion region at Earth's magnetopause, *Geophys. Res. Lett.*, *43*, 3042–3050, doi:10.1002/2016GL068359.
- Lindqvist, P.-A., et al. (2014), The spin-plane double probe electric field instrument for MMS, *Space Sci. Rev.*, *199*, 137–165, doi:10.1007/s11214-014-0116-9.
- Mozer, F. S., and P. L. Pritchett (2011), Electron physics of asymmetric magnetic field reconnection, *Space Sci. Rev.*, *158*, 119–143.
- Norgren, C., et al. (2016), Finite gyroradius effects in the electron outflow of asymmetric magnetic reconnection, *Geophys. Res. Lett.*, *43*, 6724–6733, doi:10.1002/2016GL069205.
- Pollock, C., et al. (2016), Fast plasma investigation for magnetospheric multiscale, *Space Sci. Rev.*, *199*, 331–406, doi:10.1007/s11214-016-0245-4.
- Pritchett, P. L. (2008), Collisionless magnetic reconnection in an asymmetric current sheet, *J. Geophys. Res.*, *113*, A06210, doi:10.1029/2007JA012930.

- Russell, C., et al. (2014), The magnetospheric multiscale magnetometers, *Space Sci. Rev.*, *199*, 189–256, doi:10.1007/s11214-014-0057-3.
- Shay, M. A., T. D. Phan, C. C. Taggerty, M. Fujimoto, J. F. Drake, K. Malakit, P. A. Cassak, and M. Swisdak (2016), Kinetic signatures of the region surrounding the X line in asymmetric (magnetopause) reconnection, *Geophys. Res. Lett.*, *43*, 4145–4154, doi:10.1002/2016GL069034.
- Shen, C., X. Li, M. Dunlop, Z. X. Liu, A. Balogh, D. N. Baker, M. Hapgood, and X. Wang (2003), Analyses on the geometrical structure of magnetic field in the current sheet based on cluster measurements, *J. Geophys. Res.*, *108*(A5), 1168, doi:10.1029/2002JA009612.
- Shi, Q. Q., C. Shen, Z. Y. Pu, M. W. Dunlop, Q. G. Zong, H. Zhang, C. J. Xiao, Z. X. Liu, and A. Balogh (2005), Dimensional analysis of observed structures using multipoint magnetic field measurements: Application to Cluster, *Geophys. Res. Lett.*, *32*, L12105, doi:10.1029/2005GL022454.
- Sonnerup, B., and M. Scheible (1998), Minimum and maximum variance analysis, in *Analysis Methods for Multi-Spacecraft Data*, *ISSI Sci. Rep. SR-001*, edited by G. Paschmann and P. Daly, pp. 185–220, Int. Space Sci. Inst, Bern, Switz.
- Speiser, T. W. (1965), Particle trajectories in model current sheets: 1. Analytical solutions, *J. Geophys. Res.*, *70*(17), 4219–4226, doi:10.1029/JZ070i017p04219.
- Torbert, R., et al. (2014), The fields instrument suite on MMS: Scientific objectives, measurements, and data products, *Space Sci. Rev.*, *199*, 105–135, doi:10.1007/s11214-014-0109-8.
- Wang, S., et al. (2016a), Ion demagnetization in the magnetopause current layer observed by MMS, *Geophys. Res. Lett.*, *43*, 4850–4857, doi:10.1002/2016GL069406.
- Wang, S., et al. (2016b), Two-scale ion meandering caused by the polarization electric field during asymmetric reconnection, *Geophys. Res. Lett.*, *43*, 7831–7839, doi:10.1002/2016GL069842.
- Zenitani, S., M. Hesse, A. Klimas, and M. Kuznetsova (2011), New measure of the dissipation region in collisionless magnetic reconnection, *Phys. Rev. Lett.*, *106*, 195003, doi:10.1103/PhysRevLett.106.195003.